Journal of Advanced Ceramics
2024, **13**(6): 736–745
https://doi.org/10.26599/JAC.2024.9220892

Research Article

Well-designed g-C_3N_4 nanosheet incorporated Ag loaded $Er_{0.05}La_{0.95}FeO_3$ heterojunctions for isoamyl alcohol detection

Kaichun Xu[1], Mengjie Han[1], Zichen Zheng[1], Zexin Yu[2], Hanlin Liao[3], Hui Sun[4,✉], Chao Zhang[1,✉]

[1] *College of Mechanical Engineering, Yangzhou University, Yangzhou 225127, China*
[2] *Institute for Manufacturing Technologies of Ceramic Components and Composites (IMTCCC), University of Stuttgart, Stuttgart 70569, Germany*
[3] *ICB UMR 6303, CNRS, Univ. Bourgogne Franche-Comté, UTBM, Belfort 90010, France*
[4] *School of Space Science and Physics, Shandong University, Weihai 264209, China*

Received: December 31, 2023; Revised: March 22, 2024; Accepted: April 4, 2024

Abstract: Because the volatile content of isoamyl alcohol increases sharply on the seventh day of wheat mildew infection, isoamyl alcohol can be used as an early biomarker of wheat mildew infection. Currently, only a few sensors for isoamyl alcohol detection have been reported, and these sensors still suffer from low sensitivity and poor moisture resistance. Herein, the isoamyl alcohol sensitivity of 5 at% Er@$LaFeO_3$ (ELFO) was enhanced by loading Ag nanoparticles on the surface of the ELFO microspheres, while the optimal operating temperature was reduced. The moisture resistance of Ag/ELFO was improved by the incorporation of g-C_3N_4 nanosheets (NSs) on the surface of Ag/ELFO through electrostatic self-assembly. Given the requirements for practical applications in grain granaries, the sensing behavior of a Ag/ELFO-based sensor incorporating g-C_3N_4 NSs at 20% relative humidity (RH) was systematically studied, and the sensor demonstrated excellent repeatability, long-term stability, and superior selectivity (791 at 50 ppm) for isoamyl alcohol with a low limit of detection (LOD = 75 ppb). Furthermore, the practical results obtained for wheat at different mildew stages further confirmed the potential of the g-C_3N_4/Ag/ELFO-based sensor for monitoring the early mildew stage of wheat. This work may offer guidance for enhancing the moisture resistance of gas-sensitive materials through the strategy of employing composite nanomaterials.

Keywords: Ag; Er@$LaFeO_3$ (ELFO); g-C_3N_4 nanosheet (NS); moisture resistance; isoamyl alcohol; gas sensor

1 Introduction

The rapid nondestructive detection of wheat mold, an essential grain crop, is crucial for ensuring food safety. According to the research of Lin *et al.* [1], the content of isoamyl alcohol released from stored wheat (30 °C and 90% relative humidity (RH)) was detected by gas chromatography–mass spectrometry after 7 d ((9428±991) ppm@7 d and (21,320±279) ppm@11 d), making it a potential biomarker for the early stage of wheat mildew. Due to the advantages of e-noses, such as the ability to recognize multiple components, a rich array of sensing elements, and high integration, their applications for rapid and nondestructive detection of complex and diverse biomarkers in the spoilage of grains, meat, and other foods has been widely studied [2]. The development of chemiresistive gas sensors, a core component influencing the recognition capability of electronic noses, has garnered significant attention [3]. Currently, there is a scarcity of chemiresistors for isoamyl alcohol detection, which suffers from low sensitivity [4–6]. Vioto *et al.* [4] prepared flower-like NiO assembled from nanosheets, and the sensor exhibited a certain sensitivity to isoamyl alcohol (2.8@100 ppm) at 250 °C. Liu *et al.* [5] designed a CdS/MoS_2-based sensor that exhibited excellent selectivity for isoamyl alcohol (94–100 ppm). In our previous work, $LaFeO_3$-based sensing materials demonstrated remarkable sensitivity for isoamyl alcohol [7]. However, it is essential to note that there is still potential for lowering the optimal operating temperature and enhancing moisture resistance. The Chinese national standards for the moisture content for safe grain storage clearly indicate that the storage moisture in wheat storage warehouses should be maintained below 14% to avoid melting.

Loading noble metal particles (Pt, Au, and Ag) on the surface of metal oxide semiconductors (MOSs) has proven to be an effective strategy for reducing the optimal operating temperature [8], among which Ag-containing materials are generally favored by gas sensor developers due to their lower cost. To enhance moisture resistance, multiple strategies have been investigated, including incorporating special micro/nanostructures into sensing materials [9], doping or loading noble metal nanoparticles for material modification [10,11], creating hydrophilic/sensing material heterojunctions [12], and applying hydrophobic material layers on the surface of sensing coatings [13]. Preparing a double-layer coating is a straightforward strategy to hinder the generation of OH groups, but the process is often more complex, and the sensitivity may be reduced. Impressively, Jeong *et al.* [13] deposited a Tb_4O_7 overlayer on In_2O_3 sensors, effectively eliminating the dampening effect of humidity on gas-sensitive performance without significantly changing the sensitivity, selectivity, or baseline resistance of the sensors. Doping lanthanum

✉ Corresponding authors.
E-mail: H. Sun, huisun@sdu.edu.cn;
C. Zhang, zhangc@yzu.edu.cn

[14] or loading the corresponding metallic oxidation ceramics and noble metal particles [15] are significant strategies for enhancing moisture resistance because of the significant variation in selectivity and deterioration of sensitivity. Qin *et al.* [16] fabricated a sensor based on nano-Ag&ZIF-8 comodified silicon nanowires (SiNWs), and the sensor exhibited enhanced moisture resistance, which was attributed to the synergistic effect of the hydrophobicity of the modified ZIF-8 and the hygroscopic center formed by Ag nanoparticles. Furthermore, the amalgamation of nanomaterials with metal oxides may mitigate the deterioration of water molecules on the sensitivity [17,18]. Polymers with nanostructures (such as g-C_3N_4 nanosheets (NSs)) usually possess a relatively robust capacity for the adsorption and desorption of water molecules [19,20], which may enhance the moisture resistance of MOS-based sensors. Chen *et al.* [21] reported g-C_3N_4/SnO_2-based sensors with superior sensitivity to NO_2 and excellent moisture resistance, which were prepared by pyrolysis with a g-C_3N_4 template.

As indicated by our prior research [7], the incorporation of 5 at% Er contributed to the optimal enhancement of the isoamyl alcohol sensing performance of the $LaFeO_3$-based sensor. Based on this, we designed Ag-loaded ELFO heterojunctions incorporating g-C_3N_4 NSs to lower the optimal temperature and enhance the isoamyl alcohol sensing performance at high relative humidity (RH). According to the humidity requirements of wheat storage, the sensing properties of g-C_3N_4/Ag/ELFO at 20% RH were systematically investigated, and the results indicated the superior practicability of g-C_3N_4/Ag/ELFO in large grain warehouses [7], which could be attributed to the spillover effect of Ag nanoparticles and the enhanced contact angle caused by the g-C_3N_4 incorporation.

2 Experiment

Chemical reagents are provided in the Electronic Supplementary Material (ESM). Urea (0.5 g) was added to a crucible with a lid, and yellow g-C_3N_4 powder was obtained after calcination at 550 °C (4 °C/min) for 3 h. The obtained g-C_3N_4 was dispersed ultrasonically in isopropyl alcohol for 30 min and subsequently filtered and dried at 60 °C.

Ag-loaded ELFO and g-C_3N_4/Ag-loaded ELFO heterojunctions were prepared by simple hydrothermal method combined with electrostatic self-assembly. Ag-loaded ELFO (molar ratios of Ag:$LaFeO_3$ of 0.5%, 1%, 1.5%, and 2%) was prepared by adding x mL of 0.085 M $AgNO_3$ standard solution to the Er–La–Fe nitrate–citric acid precursor (Er : La : Fe = 0.05 : 0.95 : 1). $Er(NO_3)_3{\cdot}6H_2O$ (0.2 mmol), $La(NO_3)_3{\cdot}6H_2O$ (3.8 mmol), $Fe(NO_3)_3{\cdot}9H_2O$ (4 mmol), and critic acid (24 mmol) were successively dissolved in 40 mL of distilled (DI) water with the addition of x mL of $AgNO_3$ standard solution, which was stirred at room temperature for 10 min to form orange sol. Subsequently, the sol was transferred into a 100-mL Teflon-lined stainless autoclave and reacted at 180 °C for 12 h. The precipitate was collected, washed three times with water and ethanol, dried at 70 °C for 12 h, and then calcined at 700 °C for 3 h. Finally, the brown Ag-loaded ELFO powders were obtained, and the samples corresponding to x = 0.235, 0.470, 0.705, and 0.940 were marked as SA0.5, SA1, SA1.5, and SA2, respectively, which were collectively designated as SA. First, 0.5, 1, 1.5, and 2 mg of g-C_3N_4 were dispersed in ethanol, followed by the addition of 0.05 g of SA1.5, vigorous stirring for 1 h, annealing at 400 °C for 2 h after drying, and the resulting products were labeled 0.5CA, 1CA, 1.5CA, and 2CA, which were collectively referred to as CA (Fig. 1). SA and CA samples (20 mg) were dispersed in 0.2 mL of DI water and ground to form slurry, which was drip-coated on an interdigital Pt electrode to fabricate gas sensors. Characterization methods and gas sensing measurements are provided in the ESM.

The response (S) was defined as $S = R_g/R_a$ based on the sensing performance of the fabricated sensors (p-type semiconductors) for isoamyl alcohol, where R_a and R_g denote the resistances in air and the target gas, respectively. The response/recovery time (τ_{res}/τ_{rec}) represented the time it took to attain a 90% change in response to the introduction or expulsion of isoamyl alcohol. To validate the practical capabilities of g-C_3N_4/Ag-loaded ELFO heterojunctions for wheat mildew identification, tests were conducted on composite materials with optimal performance, which focused on their response behavior to wheat with different degrees of mildew. The specific experimental process is described in the ESM.

3 Results and discussion

3.1 Characterization results

The XRD patterns of the SA, CA, and g-C_3N_4 samples are shown

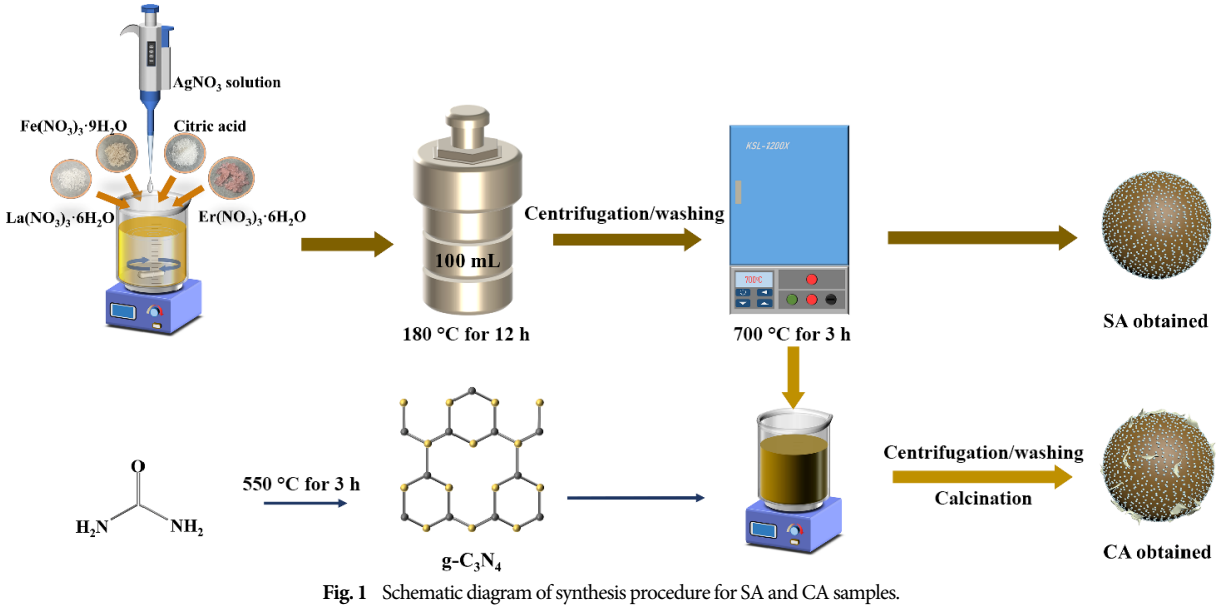

Fig. 1 Schematic diagram of synthesis procedure for SA and CA samples.

清華大学出版社 Tsinghua University Press | SciOpen

in Figs. 2(a) and 2(b). The characteristic diffraction peaks located at approximately 22.6°, 32.2°, 39.7°, 46.2°, 57.4°, 67.3°, and 76.5° correspond to the (002), (112), (022), (004), (204), (040), and (116) crystal planes of orthorhombic $LaFeO_3$ (PDF#74-2203) [22], respectively, demonstrating the excellent crystallinity of the samples. With the addition of the $AgNO_3$ standard solution, peaks at 38.12° and 44.30° emerge, which correspond to the (111) and (200) crystal facets of Ag (PDF#04-0783) [23]. Using the Debye–Scherrer formulation (Eq. (S1) in the ESM), the grain sizes of the ELFO components in SA0.5, SA1, SA1.5, and SA2 samples were obtained to investigate the role of $AgNO_3$ in the growth of ELFO grains, and the grain sizes of the SA samples decreased (from 34.69 to 28.56 nm) with increasing $AgNO_3$ addition, as shown in Table S1 in the ESM, implying that Ag^+ ions in the reaction precursor may hinder the growth of the ELFO grains. The peaks belonging to g-C_3N_4 are not obvious in the XRD patterns of 0.5CA, 1CA, and 2CA due to the low concentration and the milder peak shape of g-C_3N_4 [24].

To investigate the incorporation of g-C_3N_4, the Fourier-transform infrared (FT-IR) spectra of the samples were examined (Fig. 2(c)). The peaks at 434.2, 544.9, 1363.2, and 1491.1 cm^{-1} correspond to the Er–O bond, the tensile vibration of the Fe–O bond in the octahedral FeO_6 group [25], the vibration of the La–O bond [26], and the asymmetric stretching of the La–C bond [27], respectively. The FT-IR spectra of the SA samples did not exhibit new characteristic peaks or significant differences with increasing amounts of Ag. For the g-C_3N_4-composited SA samples and g-C_3N_4 NSs (Fig. S1(a) in the ESM), the peaks at 812.9 and 1200–1700 cm^{-1} (1252.5, 1326.3, 1567.2, and 1633.5 cm^{-1}) align with the skeleton vibration of triazine rings and the stretching and contraction vibration of C–N heterocycles of triazole rings, respectively [28]. The peaks at 3050–3600 cm^{-1} refer to the N–H bond on the CN ring and the broad O–H stretching vibrations of the absorbed hydroxyl groups [29], which are sharper with increasing g-C_3N_4 recombination.

The morphologies of the SA samples indicate that the nanoparticles grew on the ELFO microspheres with increasing $AgNO_3$ solution injection, as shown in Figs. 3(a)–3(d). The mapping results of SA1.5 verify that Er, La, Fe, and O are distributed evenly and that Ag is distributed on the surface of the microspheres as discontinuous dots (Fig. S2 in the ESM), implying that the Ag nanoparticles were successfully loaded on the surface of ELFO. The SEM images of the g-C_3N_4 and CA samples are shown in Fig. S3 in the ESM and Figs. 3(e)–3(h), which indicate that g-C_3N_4 effectively composited the Ag-loaded Er-doped $LaFeO_3$. The energy dispersive X-ray spectroscopy (EDX) results of the SA samples revealed the atomic ratios of Ag, Er, La, Fe, and O (Table S2 in the ESM). The Er : ((La + Fe)/2) atomic ratios of the SA and CA samples are close to 5%, and the Ag : ((La + Fe)/2) atomic ratios of the SA0.5, SA1, SA1.5, SA2, 0.5CA, 1CA, 1.5CA, and 2CA samples are 0.46%, 1.00%, 1.48%, 1.94%, 1.47%, 1.50%, 1.62%, and 1.45%, respectively (Fig. S1(b) in the ESM). Moreover, the mass ratios of C and N increase with increasing g-C_3N_4 incorporation (Table S3 in the ESM). As exhibited in Fig. 3(i), g-C_3N_4 NSs are dispersed across the surface of EFLO loaded with Ag nanoparticles. According to the local magnified images (red frame) of the high-resolution transmission electron microscopy (HRTEM) image of 1CA (Fig. 3(j)), Figs. 3(k) and 3(l) correspond to the (002) crystal face of g-C_3N_4 and the (111) crystal face of Ag, respectively [29,30]. Furthermore, the elemental distribution of 1CA is depicted in Figs. 3(m)–3(t), which is compatible with Fig. S2 in the ESM.

X-ray photoelectron spectroscopy (XPS) was performed to determine the valence stage of Ag, Er, La, and Fe. Figure 4(a) shows the survey spectra of SA, where the Ag 3d, Er 4d, La 3d, Fe 2p, and Fe 3p peaks are distinct. CA samples were obtained by incorporating g-C_3N_4 with prepared SA1.5. Therefore, a peak corresponding to the N 1s region emerges in the survey spectra of the CA samples, as shown in Fig. 4(b). The SA1.5 spectrum was used to analyze the peak-fitting results of each element. The peaks located at 710.2, 712.0, 718.9, 724.2, and 727.0 eV in the Fe 2p region correspond to the Fe $2p_{3/2}$, Fe $2p_{3/2}$ satellite, Fe $2p_{1/2}$, and Fe $2p_{1/2}$ satellite, respectively, which implies the presence of Fe^{3+} (Fig. 4(c) and Table S4 in the ESM). The Fe 3p peaks in Figs. 4(a) and 4(b) indicate the presence of Fe^{2+}, which originates from the reduction of Fe^{3+} caused by the lattice distortion caused by Er^{3+}

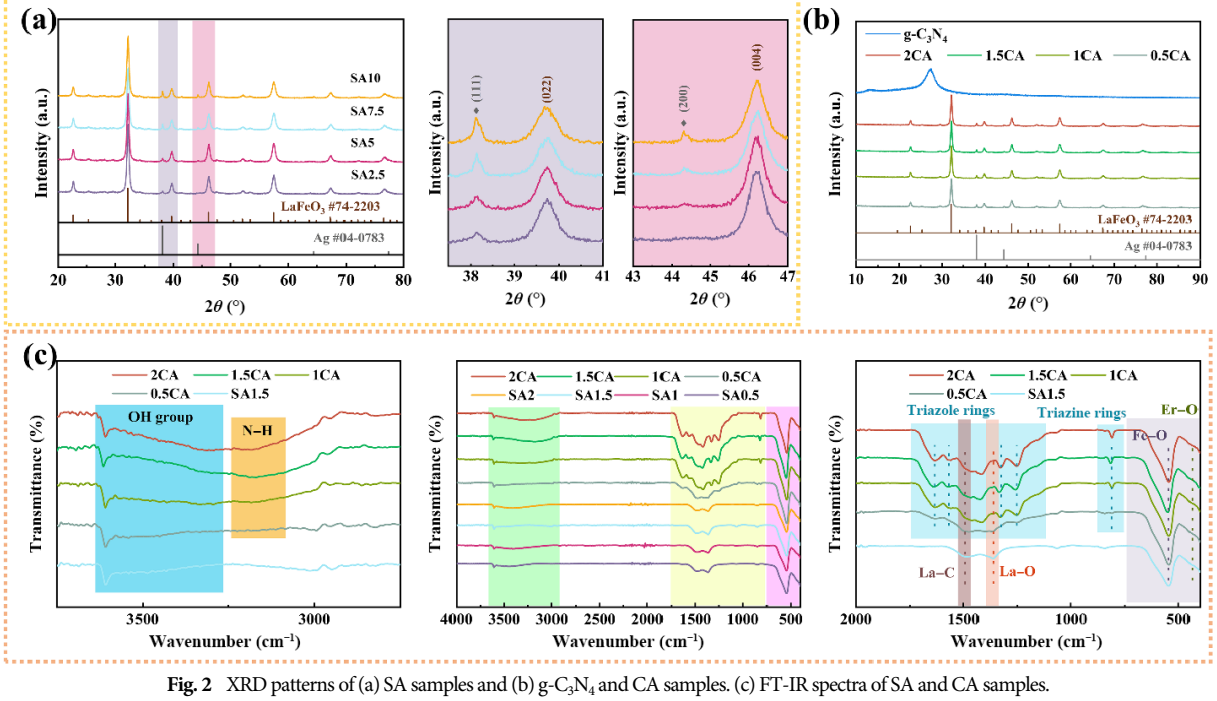

Fig. 2 XRD patterns of (a) SA samples and (b) g-C_3N_4 and CA samples. (c) FT-IR spectra of SA and CA samples.

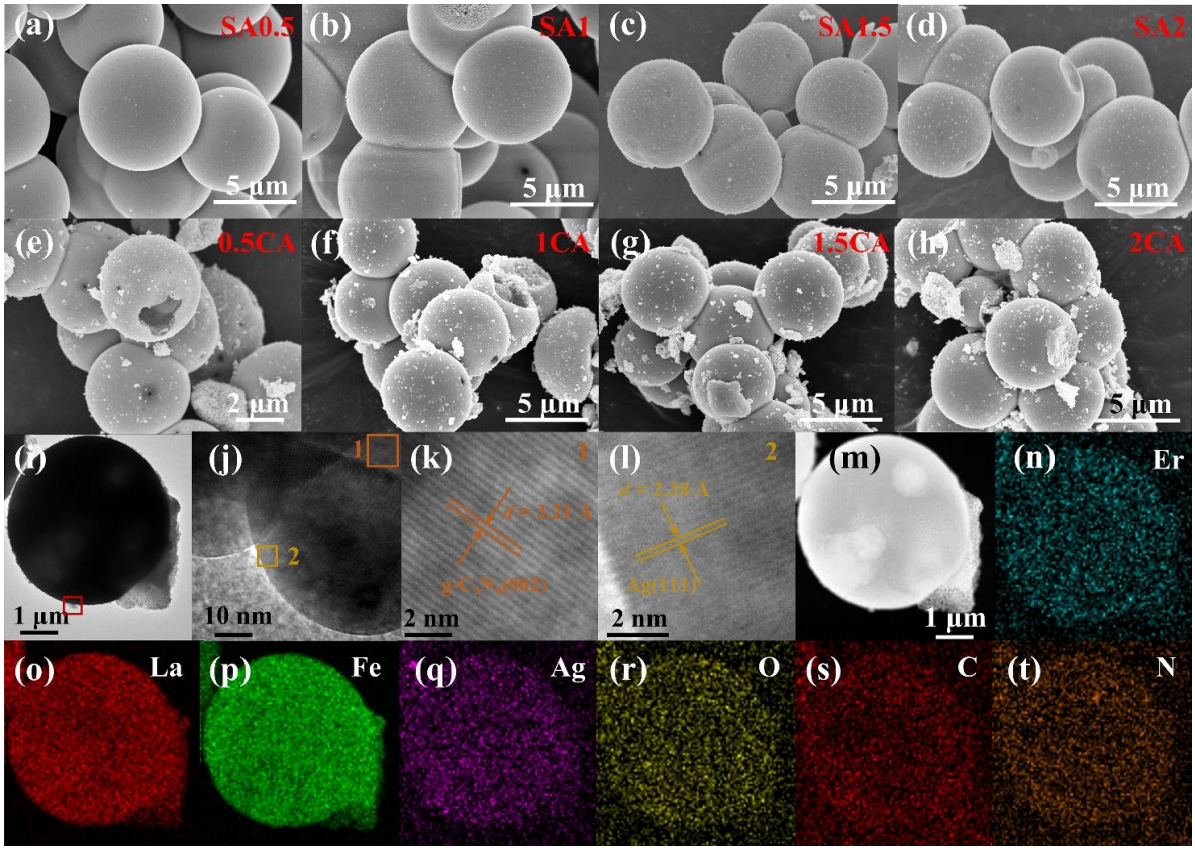

Fig. 3 SEM images of (a) SA0.5, (b) SA1, (c) SA1.5, and (d) SA2; SEM images of (e) 0.5CA, (f) 1CA, (g) 1.5CA, and (h) 2CA; (i) TEM, (j–l) HRTEM, (m) high-angle annular dark-field scanning TEM (HAADF-STEM) images, and (n–t) EDX elemental mappings of 1CA.

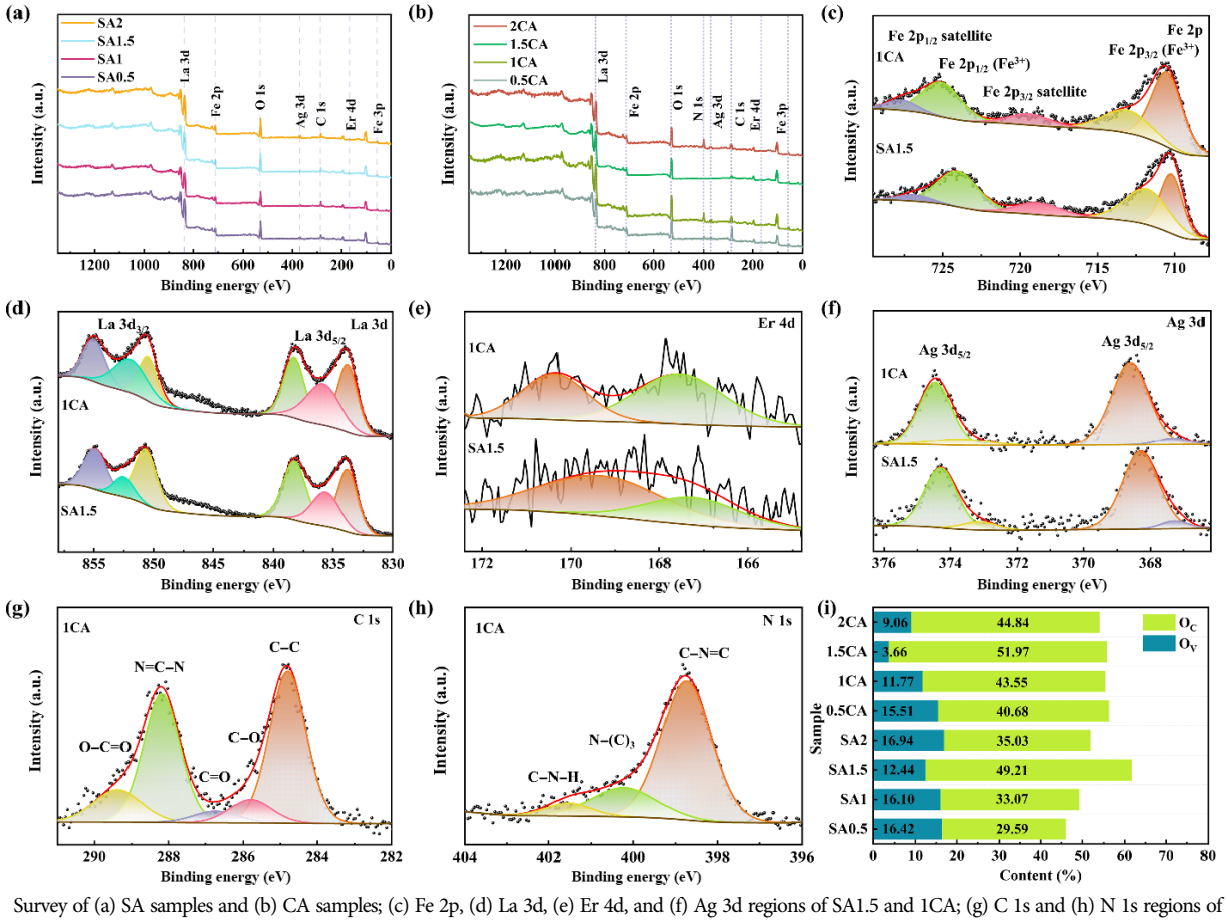

Fig. 4 Survey of (a) SA samples and (b) CA samples; (c) Fe 2p, (d) La 3d, (e) Er 4d, and (f) Ag 3d regions of SA1.5 and 1CA; (g) C 1s and (h) N 1s regions of 1CA; (i) concentrations of O_V and O_C in SA and CA samples.

清華大学出版社 Tsinghua University Press | SciOpen

doping. The fitting results and locations of the peaks in the La 3d and Er 4d regions are illustrated in Figs. 4(d) and 4(e) and Table S5 in the ESM, confirming the presence of La^{3+} and Er^{3+} valence states [31]. The peaks at 368.3 and 374.3 eV originate from Ag $3d_{5/2}$ and Ag $3d_{3/2}$, respectively, which indicates that a significant amount of Ag^0 was loaded on the surface of the SA and CA samples (Fig. 4(f)) [32]. In contrast, the peaks at 367.3 and 373.1 eV correspond to the Ag^+ generated from the oxidization of Ag during calcination, indicating that part of the Ag^+ was doped into the lattice of ELFO [33]. Notably, the majority of the binding energies of the fitted peaks based on the XPS spectra of 1CA are greater than those of the SA1.5 samples (Tables S4–S6 in the ESM). The transfer of electrons from g-C_3N_4 to Ag/ELFO reduces the carrier concentration and causes the peak to shift to a high energy [24], implying strong interactions between SA1.5 and g-C_3N_4 [28]. The C 1s region can be divided into five peaks located at 284.8, 285.8, 286.7, 288.2, and 289.4 eV, which correspond to C–C, C–O, C=O, N=C–N, and O–C=O, respectively [34] (Fig. 4(g)). As shown in Fig. 4(h), the peaks located at 398.7, 400.3, and 401.6 eV are related to C–N=C, N–$(C)_3$, and C–N–H in g-C_3N_4 [35]. The O 1s region of the SA and CA samples was fitted to three peaks corresponding to lattice oxygen (O_L), oxygen vacancy (O_V), and chemisorbed oxygen (O_C) (Figs. S4(a) and S4(b) in the ESM), and the ratios of various oxygen types for the SA and CA samples are visually shown in Fig. 4(i). The increase in the O_V and O_C proportions contributes to the increase in the sensitivity, which is consistent with the subsequent sensing results of each sample to isoamyl alcohol. In summary, in a typical crystal structure of CA, La at the A-site is substituted by Er, and Ag nanoparticles are loaded onto the surface of the ELFO crystal; there is a close integration between g-C_3N_4 and Ag/ELFO.

3.2 Gas sensing performance

To study the roles of Ag loading and g-C_3N_4 recombination on the isoamyl alcohol sensing performance of ELFO, we evaluated the sensitivity of SA and CA to 50 ppm isoamyl alcohol at various temperatures without the introduction of wet air (Fig. 5(a)). For the SA samples, the highest response emerges for the SA samples injected with more $AgNO_3$ solution at a lower operating temperature. However, the low-temperature detection has fatal shortcomings in terms of gas sensing performance: The increase in τ_{res}/τ_{rec} (Fig. 5(b)) indicates that the time needed to restore the resistance to the original baseline resistance increases. The highest response of 0.5CA to 50 ppm isoamyl alcohol appears at 200 °C, while those of 1CA and 2CA appear at 225 °C, which results from the higher energy barrier of carrier transfer caused by the heterojunction between g-C_3N_4 and SA1.5. The lower sensitivity of CA sensors can be attributed to the synergistic effect of a higher carrier transfer barrier, lower specific surface area, and weakening of silver sensitization caused by the coverage of g-C_3N_4 nanosheets. The effects of temperature on the sensitivity of the SA and CA samples and the response-recovery speed of SA1.5 were taken into account, and 225 °C was determined to be the optimal operating temperature. The response values of the CA samples decrease with increasing the g-C_3N_4 incorporation.

Figure 5(c) illustrates the responses and baseline resistances of the SA1.5, 0.5CA, 1CA, and 2CA sensors to 50 ppm isoamyl alcohol at various RHs. Water molecules adsorbed on the surface of gas-sensitive materials hinder the adsorption and charge transfer of the target gas molecules on the surface of the materials and the diffusion process inside the sensing coating. Moreover, water molecules have a negative effect on the preadsorption process of oxygen molecules (O_2). Thus, there is an associated

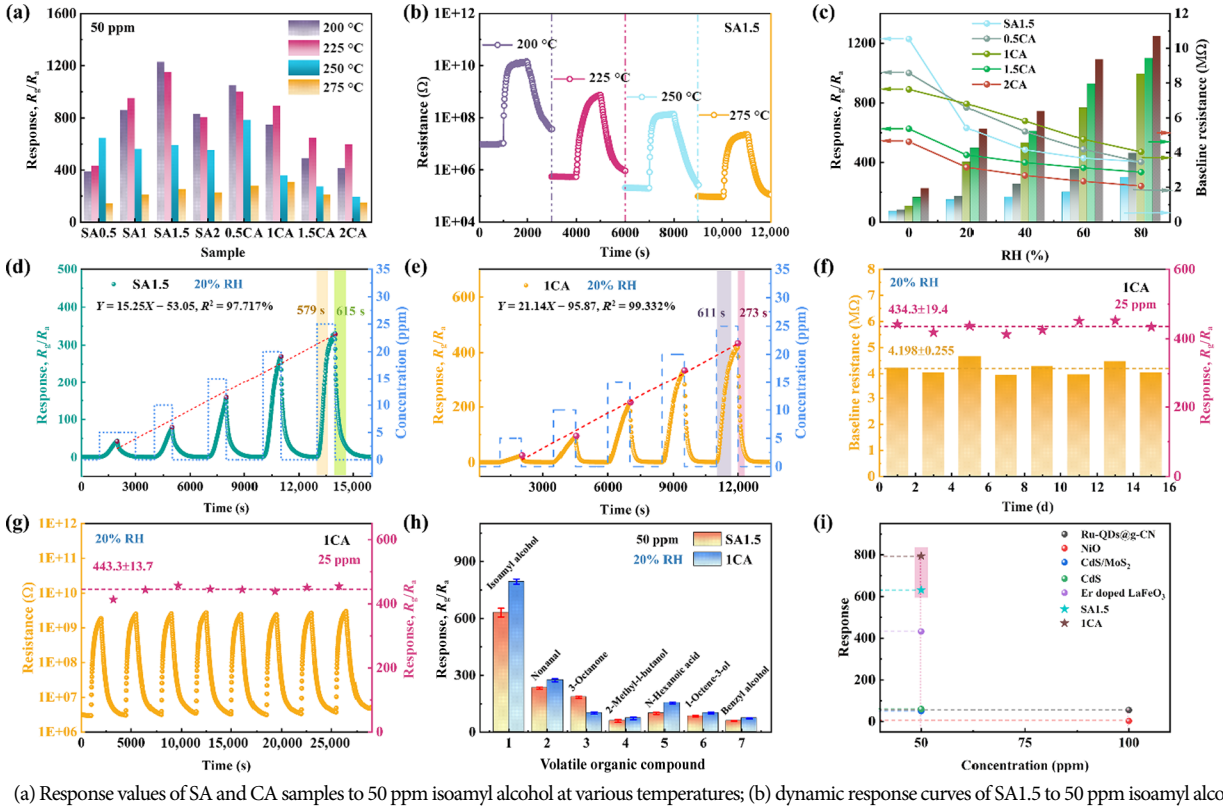

Fig. 5 (a) Response values of SA and CA samples to 50 ppm isoamyl alcohol at various temperatures; (b) dynamic response curves of SA1.5 to 50 ppm isoamyl alcohol at various temperatures; (c) response and baseline resistance values of SA1.5, 0.5CA, 1CA, 2CA to 50 ppm isoamyl alcohol with various RHs (0–80%) at 225 °C; dynamic response curves and linear relationship between response and isoamyl alcohol concentrations (5–25 ppm) of (d) SA1.5 and (e) 1CA; (f) long-term (15 d) stability and (g) repeatable characteristics of 1CA; (h) selectivity of SA1.5 and 1CA to 50 ppm VOCs generated from mildew wheat; (i) isoamyl alcohol sensing performance of this work and research works reported.

increase in baseline resistance and a concurrent decrease in response to the increase in RH. As the amount of g-C_3N_4 composite increases, the baseline resistance of CA gradually increases, and heterojunction regions are formed at the interface between SA1.5 and g-C_3N_4, resulting in an increased contact area and numerous potential barriers that hinder hole transport [12]. Consequently, it results in the formation of depletion and accumulation layers of holes on both sides of the interface, which causes a reduced carrier concentration and an increased baseline resistance of CA. Excitingly, with increasing g-C_3N_4 composite concentration, although the sensor's response decreases slightly, its resistance to humidity increases remarkably. To establish a clear criterion of moisture resistance, the ratio of the response at the x% RH level (S_{xRH}) to the response at 0% RH (S_{0RH}) was defined as MR_x. MR_{20}, MR_{40}, MR_{60}, and MR_{80} of SA1.5 are 51.42%, 39.78%, 34.94%, and 32.97%, respectively. In contrast, MR_{20}, MR_{40}, MR_{60}, and MR_{80} of the 1CA sensor are 89.17%, 76.18%, 62.41%, and 52.90%, respectively, which indicates a significant enhancement in moisture resistance for the SA1.5 sensor after the incorporation of the 1% g-C_3N_4 composite. Based on the application background, sensing measurements of SA1.5 and 1CA at 20% RH were carried out.

The dynamic response curves of SA1.5 and 1CA are exhibited in Figs. 5(d) and 5(e), which illustrate the response values to 5–25 ppm isoamyl alcohol, the linearity between the response value and target gas concentration, and the τ_{res}/τ_{rec} to 25 ppm isoamyl alcohol. Benefiting from the improved moisture resistance, the response values of 1CA at 20% RH to concentrations of 5–25 ppm are 25.27, 95.38, 216.21, 335.98, and 423.55, implying superior linearity (the slope is 21.14 with a high correlation coefficient (R^2 = 99.332%)). These values surpass those of SA1.5 under the same conditions, which are 42.15, 79.51, 158.98, 269.91, and 328.32, respectively. τ_{res} of 1CA isoamyl alcohol is 611 s, which is longer than that of SA1.5 (579 s). τ_{rec} of 1CA to 25 ppm target gas is 273 s, which is faster than that of SA1.5 (615 s). Based on the slopes of the two sensors obtained in Eqs. (1) and (2), LODs of SA1.5 and 1CA can be obtained [36].

$$\mathrm{RMS_{noise}\ (ppm)} = (\Sigma(r - r_i)^2/N)^{0.5} \quad (1)$$

$$\mathrm{LOD} = 3\mathrm{RMS_{noise}}/k \quad (2)$$

where k, r, r_i, and N represent the slope (log(S − 1)–log(the concentration of target gas)), the baseline response data, the average value, and the number of points taken (50), respectively. LODs of SA1.5 and 1CA were determined to be 126 and 75 ppb, respectively.

The response to 25 ppm isoamyl alcohol for 15 d is stable at 434.3, with a low standard deviation of 19.4. Additionally, the baseline resistance for 15 d is consistently maintained at (4.198±0.255) MΩ, indicating the excellent long-term stability of 1CA (Fig. 5(f)). The dynamic 8-cycle response curve of 1CA at 20% RH exhibits impressive repeatability (S = 443.3±13.7@ 25 ppm), as depicted in Fig. 5(g). To evaluate the selectivity of SA1.5 and 1CA, the response values to 50 ppm of various VOCs were measured at 20% RH, all of which exhibit increased volatility during the wheat mold growth process. As illustrated in Fig. 5(h), both SA1.5 and 1CA exhibit outstanding selectivity for isoamyl alcohol. Moreover, Fig. 5(i) visually contrasts the sensitivity of SA1.5 and 1CA in this study to chemical resistive sensors previously reported for isoamyl alcohol gas, confirming the superior sensing properties of SA1.5 and 1CA in this work to isoamyl alcohol, as shown in Table S7 in the ESM.

3.3 Gas sensing mechanism

The isoamyl alcohol sensing mechanism of $LaFeO_3$-based gas-sensitive coatings can be divided into two stages: (1) O_2 is pre-adsorbed on the coating surface at high temperature, which generates oxygen anions (O_2^- and O^-) and a hole accumulation layer (HAL) (Fig. 6(a)) [10]; (2) isoamyl alcohol reacts with oxygen ions, and electrons return to the coating (Eq. (3) and Fig. 6(b)) [6].

$$C_5H_{12}O_{(ads)} + 15O^-_{(ads)} \leftrightarrow 5CO_2 + 6H_2O + 15e^- \quad (3)$$

The enhanced sensing performance facilitated by Ag

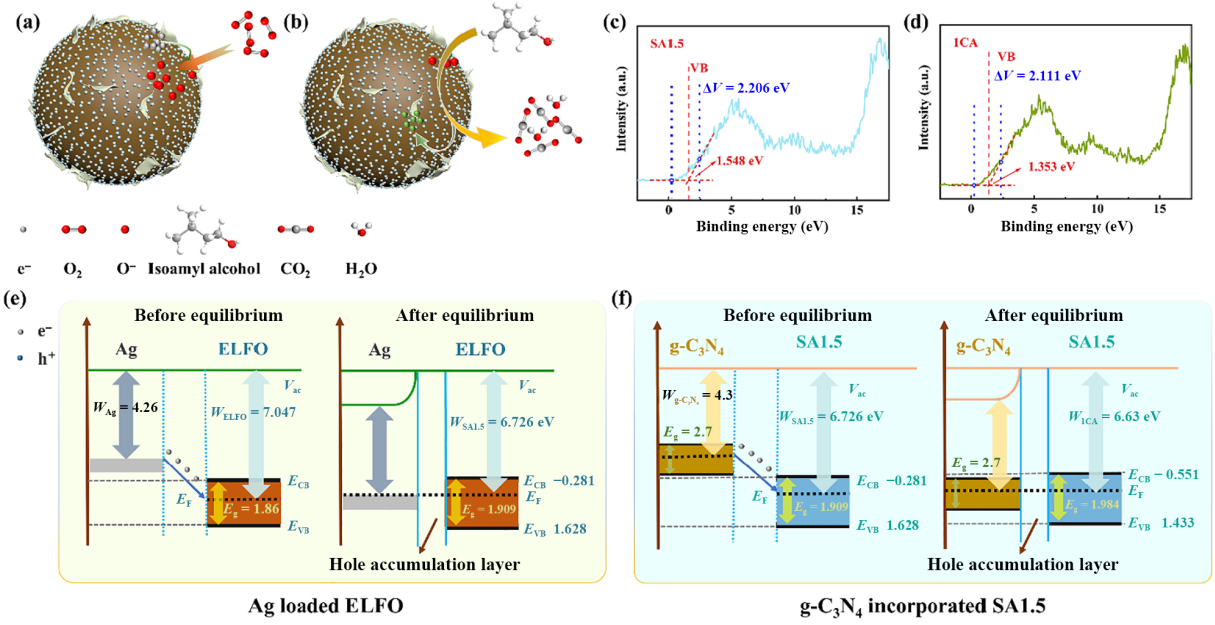

Fig. 6 Schematic illustration of (a, b) the gas-sensing mechanism of CA sensor when exposed to air and isoamyl alcohol; valence band spectra of (c) SA1.5 and (d) 1CA; band structures of (e) SA1.5 and (f) 1CA before and after equilibrium.

nanoparticles can be predominantly attributed to chemical sensitization and electronic sensitization [37]. In this process, Ag nanoparticles serve as catalytic sites, effectively reducing the adsorption activation energy and accelerating the carrier transport, thereby promoting gas reactions. The catalytic activity, spillover effect, and reduced adsorption activation energy result in a higher preadsorbed oxygen concentration on the SA1.5 surface, increasing the quantity of O^- ions and consequently enhancing the response [38]. Moreover, the lower activation energy allows gas molecules to achieve optimal thermodynamic and kinetic conditions for adsorption and desorption at relatively lower temperatures [39].

To determine the band structures of SA1.5 and 1CA, the work functions (Φ_s) for isoamyl alcohol detection and the energy bands (E_g), valence band potentials ($E_{VB,NHE}$, where VB and NHE refer to valence band and standard hydrogen electrode relative vacuum level respectively), and conduction band potentials ($E_{CB,NHE}$, where CB refers to conduction band) of SA1.5 and 1CA were determined by Eqs. (4)–(6) [36]. Based on the difference in the work functions (W_f) of Ag (W_{Ag} = 4.26 eV) and ELFO (W_{ELFO} = 7.047 eV), electrons from the loaded Ag nanoparticles are released to the valence band of ELFO [39], establishing a Fermi level equilibrium at their interface, as illustrated in Figs. 6(c) and 6(e) and Table S8 in the ESM. The formation of the Ag/ELFO heterojunction shrinks HAL, which favors the formation of preadsorbed oxygen [40]. The electron transfer process from Ag nanoparticles into the conduction band of ELFO increases the band gap of the SA samples, which is obtained by Eq. (S2) in the ESM, as shown in Figs. S4(c) and S4(d) in the ESM. Additionally, XPS spectra confirmed the existence of Ag^+, which is subsequently reduced to Ag^0 during reactions with target gas molecules, increasing the number of participating gas molecules and enhancing carrier transfer, consequently resulting in an elevated resistance (R_g) [41]. Nonetheless, it is worth noting that when the Ag content reaches 2%, the aggregation of nanoparticles will hinder the diffusion of preadsorbed oxygen on the gas-sensitive coating surface [39]. Moreover, an excessive amount of Ag nanoparticles leads to electron conduction along the Ag nanoparticles, which in turn diminishes the response of SA2 [38]. The highest O_V and (O_V + O_C) contents of SA1.5 contributed to its superior sensitivity to isoamyl alcohol [42], as shown in Fig. 4(i).

$$E_{VB,NHE} = \varphi + E_{VB,XPS} - 4.44 \quad (4)$$

$$\Delta V = \Phi - \varphi \quad (5)$$

$$E_g = E_{VB,NHE} - E_{CB,NHE} \quad (6)$$

where φ, $E_{VB,XPS}$, and ΔV represent the work function of the XPS analyzer (4.52 eV), the valence band potential calculated from VB-XPS, and the potential difference, respectively.

The g-C_3N_4 composite had two primary effects on SA1.5: weakening the sensitivity and enhancing the resistance to moisture. As depicted in Fig. 6(d), the work function of g-C_3N_4 (4.3 eV) is lower than that of SA1.5 (6.726 eV), which is similar to the change in the band structure that occurs in the Ag-ALFO composite. The transfer of electrons from g-C_3N_4 into the conduction band of SA1.5 contributes to the higher E_g (1.984 eV) and lower W_f (6.631 eV) of the CA samples (Fig. 6(f)), which theoretically should increase the response. However, as the amount of g-C_3N_4 added increases, the increase in the contact area of the g-C_3N_4 and SA1.5 heterojunctions increases the carrier transfer barrier, leading to an increase in the baseline resistance, a

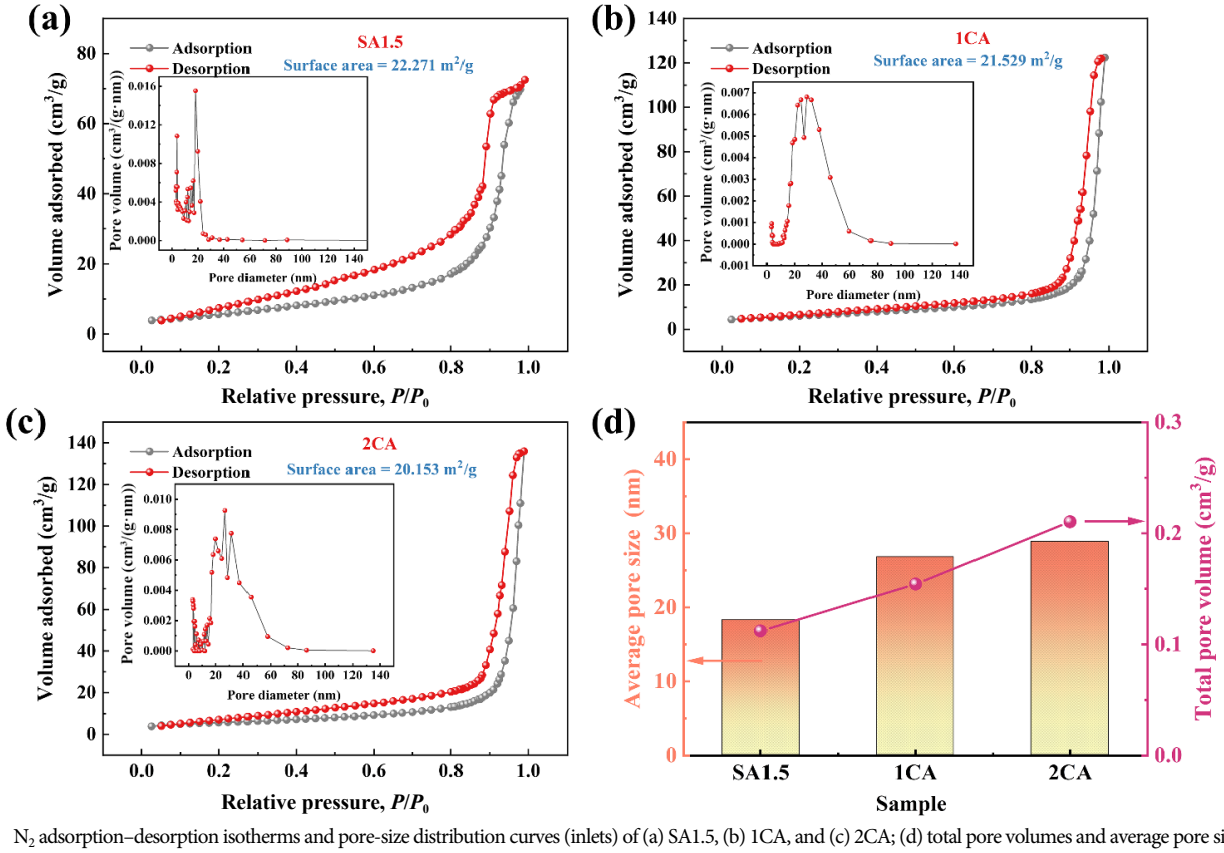

Fig. 7 N_2 adsorption–desorption isotherms and pore-size distribution curves (inlets) of (a) SA1.5, (b) 1CA, and (c) 2CA; (d) total pore volumes and average pore sizes of SA1.5, 1CA, and 2CA.

decrease in the carrier transfer, and a poor response of the sensor. Additionally, when the CA sensors were stable in synthesized air, the electron transfer from g-C_3N_4 (n-type) to pre-adsorbed O_2 increased the baseline resistance. According to the definition of response values, an increase in R_a may have a negative effect on the response. When the reducing target gas is introduced, some of the electrons that initially enter the valence band of SA1.5 are transferred to g-C_3N_4, thereby reducing the resistance of the CA samples to isoamyl alcohol and decreasing the response. Furthermore, as revealed by XPS and Brunauer–Emmett–Teller (BET) characterizations, an increase in the contact area decreases the (O_V + O_C) ratio and specific surface area in the CA samples (Figs. 4(i) and 7). This discrepancy is attributed to the surface-loaded g-C_3N_4 NSs covering the oxygen vacancy sites, which impedes the formation of oxygen ions and the sensing process. Moreover, we hypothesized that the decrease in the sensitivity of SA1.5 caused by the introduction of g-C_3N_4 NSs may also be related to the hindrance of g-C_3N_4 NSs in the sensitivity optimization of Ag particles (spillover effect). To explore the reasons for the improvement in the moisture resistance of g-C_3N_4, contact angle tests were carried out on the SA1.5, 0.5CA, 1CA, and 2CA samples, which exhibited moisture resistance values of 19.395°±0.035°, 26.58°±0.95°, 35.68°±0.73°, and 47.525°±1.735°, respectively (Fig. S5 in the ESM). Furthermore, we conducted FT-IR characterization on the sensors stabilized at 0% RH and 20% RH (225 °C) to further explain the increase in moisture resistance after the introduction of g-C_3N_4 (Fig. 8). For 1CA, after stabilizing at 20% RH, there was no significant difference in the intensity of the peak corresponding to hydroxyl groups compared to that in the spectrum of 1CA–0% RH. However, for SA1.5 stabilized at 20% RH, there was a noticeable increase in the intensity of the peak corresponding to hydroxyl groups compared to that in the spectrum of SA1.5–0% RH. This suggests that moist air is more prone to generating hydroxyl groups on the surface of the SA1.5 sensor than is 1CA at the operating temperature, and its active sites for gas sensing are more easily occupied by water molecules, leading to a deterioration in sensitivity [43].

3.4 Wheat mildew detection

The response curves of CA1 to the complex volatile gases of wheat plants with different mildew degrees exhibit various shapes. The resistance curves of CA1 to VOCs released from wheat stored for the first three days first and then decrease gradually (Figs. 9(a)–9(c)), while those to VOCs generated from wheat stored for the fifth and seventh days increase monotonically (Figs. 9(d) and 9(e)). This difference can be attributed to the large change in the composition of the gas mixture. As shown in Fig. 9(f), the responses of 1CA to VOCs in wheat after different storage periods increase exponentially within 7 d as the storage period increases (18.2, 34.8, 158, 326.2, and 734.1@1, 2, 3, 5, and 7 d, respectively), which confirms the practicability of 1CA for mildew wheat monitoring.

4 Conclusions

In this study, Ag-loaded ELFO samples were prepared using a one-step hydrothermal method, and g-C_3N_4 NSs were incorporated on their surface. Ag nanoparticles on the ELFO surface improved the sensitivity of the ELFO-based sensor through the spillover effect and optimization of the band structure. Additionally, the assembled g-C_3N_4 NSs increased the electron exchange energy barrier at the interaction region between g-C_3N_4 NSs and Ag-loaded ELFO. This hindered the generation of preadsorbed oxygen and the charge exchange process between isoamyl alcohol

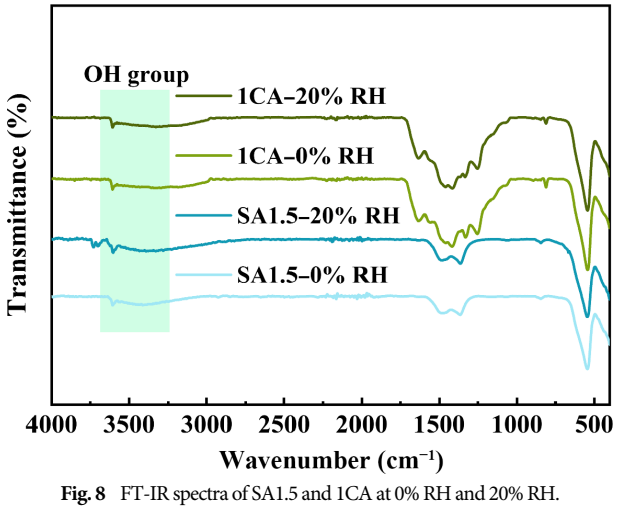

Fig. 8 FT-IR spectra of SA1.5 and 1CA at 0% RH and 20% RH.

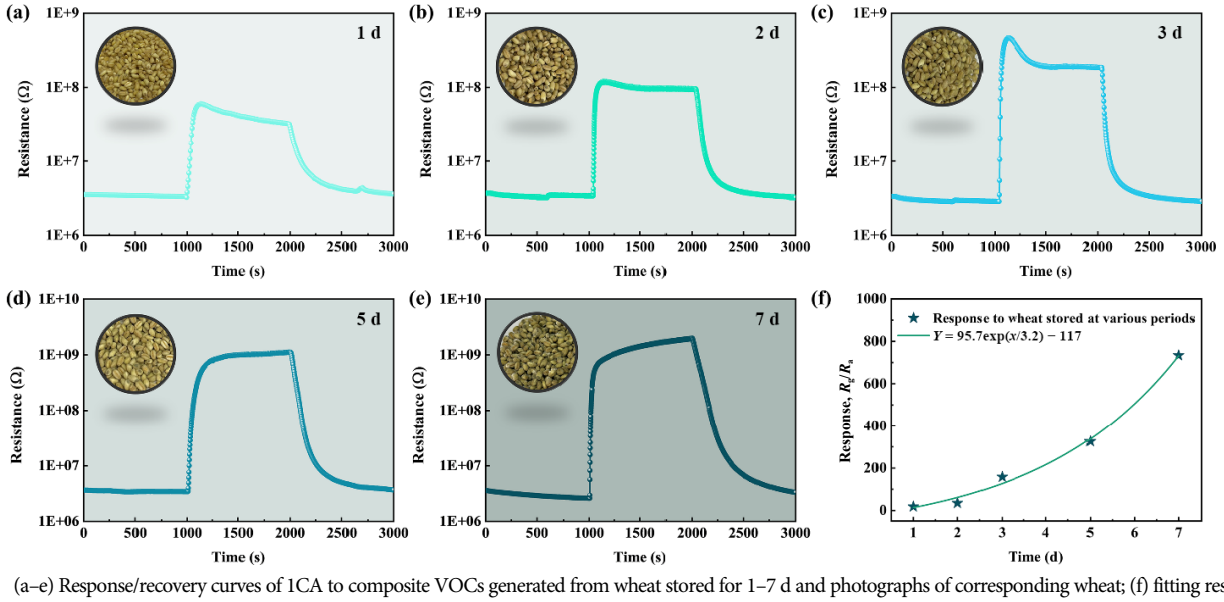

Fig. 9 (a–e) Response/recovery curves of 1CA to composite VOCs generated from wheat stored for 1–7 d and photographs of corresponding wheat; (f) fitting result of response value.

and CA samples, decreasing the sensitivity of Ag-loaded ELFO. Remarkably, although the introduction of g-C_3N_4 NSs reduced the sensitivity of the Ag-loaded ELFO-based sensor, it improved the moisture resistance of the sensor with increasing the g-C_3N_4 incorporation. This improvement is significant for the practical applications of the sensor for monitoring mildew wheat in granaries.

Acknowledgements

This work was supported by the Outstanding Youth Foundation of Jiangsu Province of China (No. BK20211548), the Qinglan Project of Yangzhou University, and the Yangzhou Science and Technology Plan Project (No. YZ2023246).

Declaration of competing interest

The authors have no competing interests to declare that are relevant to the content of this article.

Electronic Supplementary Material

Supplementary material is available in the online version of this article at https://doi.org/10.26599/JAC.2024.9220892.

References

[1] Lin H, Kang WC, Kutsanedzie FYH, *et al.* A novel nanoscaled chemo dye-based sensor for the identification of volatile organic compounds during the mildewing process of stored wheat. *Food Anal Method* 2019, **12**: 2895–2907.

[2] Zheng ZC, Zhang C. Electronic noses based on metal oxide semiconductor sensors for detecting crop diseases and insect pests. *Comput Electron Agric* 2022, **197**: 106988.

[3] Zhang DD, Fang Z, Wang L, *et al.* Controllable growth of single-crystalline zinc oxide nanosheets under ambient condition toward ammonia sensing with ultrahigh selectivity and sensitivity. *J Adv Ceram* 2022, **11**: 1187–1195.

[4] Vioto GCN, Perfecto TM, Zito CA, *et al.* Flower-like NiO for the detection of 3-methyl-1-butanol, a microbial volatile organic compound. *Mater Lett* 2023, **333**: 133641.

[5] Liu L, Yang WY, Zhang H, *et al.* Ultra-high response detection of alcohols based on CdS/MoS_2 composite. *Nanoscale Res Lett* 2022, **17**: 7.

[6] Samanta S, Srinivasan P, Rayappan JBB, *et al.* Ru quantum dots decorated graphitic carbon nitride (Ru-QDs@g-CN) for chemi-resistive sensing of 3-methyl-1-butanol at room temperature. *Sens Actuat B Chem* 2022, **368**: 132060.

[7] Xu KC, Han MJ, Zheng ZC, *et al.* Role of Er doping on isoamyl alcohol sensing performance of $LaFeO_3$ microspheres and its prospects in wheat mildew detection. *J Mater Chem A* 2023, **11**: 24939–24947.

[8] Shao JK, Sun CX, Liu HY, *et al.* Insight into Au functionalization on core–shell $LaFeO_3$ spheres for high-response and selectivity n-butanol gas sensors with DFT study. *Sens Actuat B Chem* 2023, **382**: 133506.

[9] Sun Y, Dong Z, Zhang D, *et al.* The fabrication and triethylamine sensing performance of In-MIL-68 derived In_2O_3 with porous lacunaris structure. *Sens Actuat B Chem* 2021, **326**: 128791.

[10] Zhang Y, Han S, Wang MY, *et al.* Electrospun Cu-doped In_2O_3 hollow nanofibers with enhanced H_2S gas sensing performance. *J Adv Ceram* 2022, **11**: 427–442.

[11] Liu W, Xu L, Sheng K, *et al.* A highly sensitive and moisture-resistant gas sensor for diabetes diagnosis with Pt@In_2O_3 nanowires and a molecular sieve for protection. *NPG Asia Mater* 2018, **10**: 293–308.

[12] Zhang MX, Liu K, Zhang XM, *et al.* Interfacial energy barrier tuning of hierarchical Bi_2O_3/WO_3 heterojunctions for advanced triethylamine sensor. *J Adv Ceram* 2022, **11**: 1860–1872.

[13] Jeong SY, Moon YK, Kim JK, *et al.* A general solution to mitigate water poisoning of oxide chemiresistors: Bilayer sensors with Tb_4O_7 overlayer. *Adv Funct Mater* 2021, **31**: 2007895.

[14] Kwak CH, Kim TH, Jeong SY, *et al.* Humidity-independent oxide semiconductor chemiresistors using terbium-doped SnO_2 yolk–shell spheres for real-time breath analysis. *ACS Appl Mater Inter* 2018, **10**: 18886–18894.

[15] Zhang YM, Deng ZM, Zhao JH, *et al.* Unique Pd/PdO–In_2O_3 heterostructures for the highly efficient detection of triethylamine. *J Mater Chem A* 2023, **11**: 17056–17065.

[16] Qin YX, Wang XY, Zang JS. Ultrasensitive ethanol sensor based on nano-Ag&ZIF-8 comodified SiNWs with enhanced moisture resistance. *Sens Actuat B Chem* 2021, **340**: 129959.

[17] Jiang B, Zhou TT, Zhang L, *et al.* Construction of mesoporous In_2O_3–ZnO hierarchical structure gas sensor for ethanol detection. *Sens Actuat B Chem* 2023, **393**: 134203.

[18] Niu GQ, Zhao CH, Gong HM, *et al.* NiO nanoparticle-decorated SnO_2 nanosheets for ethanol sensing with enhanced moisture resistance. *Microsyst Nanoeng* 2019, **5**: 21.

[19] Meng WQ, Wu SY, Wang XW, *et al.* High-sensitivity resistive humidity sensor based on graphitic carbon nitride nanosheets and its application. *Sens Actuat B Chem* 2020, **315**: 128058.

[20] Soltani S, Ashrafi H, Nasresfahani S, *et al.* High sensitivity portable humidity sensor based on the hydrophilic surface of carbon ring–carbon nitride nanosheets and its wireless application in respiration detection. *Appl Surf Sci* 2022, **605**: 154771.

[21] Chen C, Wei Z, Sun YY, *et al.* Trace carbon nitride-decorated SnO_2 lamella boosting ultra-high response and fast recovery of NO_2 gas at low temperature. *Sens Actuat B Chem* 2024, **403**: 135214.

[22] Xu D, Zhang YM, Deng ZM, *et al.* Metal–organic framework-derived $LaFeO_3$@SnO_2/Ag p–n heterojunction nanostructures for formaldehyde detection. *ACS Appl Nano Mater* 2022, **5**: 14367–14376.

[23] Wen J, Song ZH, Ding JB, *et al.* MXene-derived TiO_2 nanosheets decorated with Ag nanoparticles for highly sensitive detection of ammonia at room temperature. *J Mater Sci Technol* 2022, **114**: 233–239.

[24] Xu XL, Lin H, Xiao P, *et al.* Construction of Ag-bridged Z-scheme $LaFe_{0.5}Co_{0.5}O_3$/Ag_{10}/graphitic carbon nitride heterojunctions for photo-fenton degradation of tetracycline hydrochloride: Interfacial electron effect and reaction mechanism. *Adv Mater Interfaces* 2022, **9**: 2101902.

[25] Zheng ZC, Liu KW, Zhou YW, *et al.* Ultrasensitive room-temperature geranyl acetone detection based on Fe@WO_{3-x} nanoparticles in cooked rice flavor analysis. *J Adv Ceram* 2023, **12**: 1547–1561.

[26] Zhang YM, Rong Q, Zhao JH, *et al.* Boron-doped graphene quantum dot/Ag–$LaFeO_3$ p–p heterojunctions for sensitive and selective benzene detection. *J Mater Chem A* 2018, **6**: 12647–12653.

[27] Mehdizadeh P, Amiri O, Rashki S, *et al.* Effective removal of organic pollution by using sonochemical prepared $LaFeO_3$ perovskite under visible light. *Ultrason Sonochem* 2020, **61**: 104848.

[28] Zhang WJ, Ma YX, Zhu XH, *et al.* Fabrication of Ag decorated g-C_3N_4/$LaFeO_3$ *Z*-scheme heterojunction as highly efficient visible-light photocatalyst for degradation of methylene blue and tetracycline hydrochloride. *J Alloys Compd* 2021, **864**: 158914.

[29] Gao XM, Shang YY, Liu LB, *et al.* A plasmonic *Z*-scheme three-component photocatalyst g-C_3N_4/Ag/$LaFeO_3$ with enhanced visible-light photocatalytic activities. *Opt Mater* 2019, **88**: 229–237.

[30] Wang M, Zhang Y, Jin CY, *et al.* Fabrication of novel ternary heterojunctions of Pd/g-C_3N_4/Bi_2MoO_6 hollow microspheres for enhanced visible-light photocatalytic performance toward organic pollutant degradation. *Sep Purif Technol* 2019, **211**: 1–9.

[31] Li SH, Liu YK, Wu YM, *et al.* Highly sensitive formaldehyde resistive sensor based on a single Er-doped SnO_2 nanobelt. *Physica B* 2016, **489**: 33–38.

[32] Zhu PF, Hu M, Duan M, *et al.* High visible light response *Z*-scheme

Ag_3PO_4/g-C_3N_4/ZnO composite photocatalyst for efficient degradation of tetracycline hydrochloride: Preparation, properties and mechanism. *J Alloys Compd* 2020, **840**: 155714.

[33] Wang Y, Niu CG, Zhang L, *et al*. High-efficiency visible-light AgI/Ag/Bi_2MoO_6 as a Z-scheme photocatalyst for environmental applications. *RSC Adv* 2016, **6**: 10221–10228.

[34] Xu JY, Liao HL, Zhang C. $ZnSnO_3$ based gas sensors for pyridine volatile marker detection in rice aging during storage. *Food Chem* 2023, **408**: 135204.

[35] Wu KD, He XX, Ly A, *et al*. Highly sensitive and selective gas sensors based on 2D/3D Bi_2MoO_6 micro-nano composites for trimethylamine biomarker detection. *Appl Surf Sci* 2023, **629**: 157443.

[36] Wu KD, Chai HF, Xu KC, *et al*. Effect of {010} crystal facets of Bi_2MoO_6 and 1D/2D heterostructures for conductometric room temperature NH_3 gas sensors. *Sens Actuat B Chem* 2023, **376**: 132983.

[37] Barbosa MS, Suman PH, Kim JJ, *et al*. Investigation of electronic and chemical sensitization effects promoted by Pt and Pd nanoparticles on single-crystalline SnO nanobelt-based gas sensors. *Sens Actuat B Chem* 2019, **301**: 127055.

[38] Xue YY, Wang JL, Li SN, *et al*. Mesoporous Ag/In_2O_3 composite derived from indium organic framework as high performance formaldehyde sensor. *J Solid State Chem* 2017, **251**: 170–175.

[39] Yue JH, Wang L, Xu JC, *et al*. Highly improved toluene gas-sensing performance of mesoporous Ag-anchored cobalt oxides nanowires. *Adv Powder Technol* 2022, **33**: 103832.

[40] Kong DL, Niu JY, Hong B, *et al*. Ag-nanoparticles-anchored mesoporous In_2O_3 nanowires for ultrahigh sensitive formaldehyde gas sensors. *Mater Sci Eng B* 2023, **291**: 116394.

[41] Wang YL, Cui XB, Yang QY, *et al*. Preparation of Ag-loaded mesoporous WO_3 and its enhanced NO_2 sensing performance. *Sens Actuat B Chem* 2016, **225**: 544–552.

[42] Xu JY, Zhang C. Oxygen vacancy engineering on cerium oxide nanowires for room-temperature linalool detection in rice aging. *J Adv Ceram* 2022, **11**: 1559–1570.

[43] Cao S, Xu YF, Yu ZZ, *et al*. A dual sensing platform for human exhaled breath enabled by Fe-MIL-101-NH_2 metal-organic frameworks and its derived Co/Ni/Fe trimetallic oxides. *Small* 2022, **18**: e2203715.